Fourier Analysis Method for Wireless Power Transfer Coil Design

Andrew Foote[1,2], Daniel Costinett[2,4], Ruediger Kusch[3], Jason Pries[4], Mostak Mohammad[4], Burak Ozpineci[2,4]

[1]Innovation Hub Knoxville, Volkswagen Group of America
[2]The University of Tennessee, Knoxville
[3]Volkswagen Group Innovation
[4]Power Electronics and Electric Machinery Research Center, Oak Ridge National Laboratory
Knoxville, TN, USA
Email: andrew.foote@vw.com

Abstract—**Wireless power transfer (WPT) systems for Electric Vehicles (EVs) are designed to meet specifications such as stray field, power transfer, efficiency, and ground clearance. Typical design approaches include iterative analysis of predetermined coil geometries to identify candidates that meet these constraints. This work instead directly generates WPT coil shapes and magnetic fields to meet specifications and constraints through the optimization of Fourier basis function coefficients. The proposed Fourier Analysis Method (FAM) applies to arbitrary planar coil geometries and does not rely on iterative finite-element analysis (FEA) simulations. This flexibility allows for rapid design evaluation across a larger range of coil geometries and design specifications. A prototype coil is built to compare FAM outputs to experimental measurements and FEA simulations. The FAM is then used to illustrate the tradeoff of coil current and stray field for a given power level showing that the method is capable of generating optimized coil shapes to meet arbitrary field constraints.**

Index Terms—**wireless power transfer, inductive power transmission, coil design, electric vehicles, Fourier analysis**
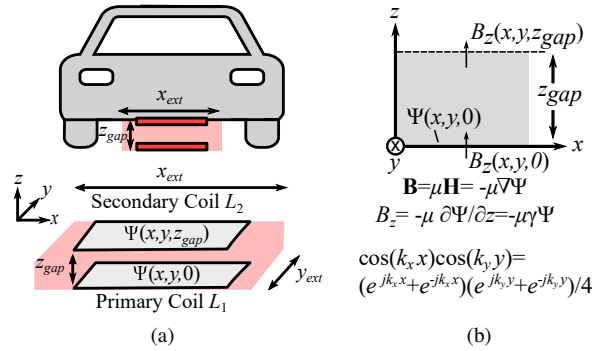
Fig. 1: (a) Illustration of the EV WPT field boundaries given by x_{ext} and y_{ext}, system airgap z_{gap} and magnetic scalar potential $\Psi(x, y, z)$ used in the Fourier Analysis Method (FAM). (b) FAM axes layout and key equations.

I. INTRODUCTION

Wireless power transfer (WPT) for Electric Vehicles (EVs) has several benefits over conductive charging including improvements in convenience, safety, automation, and vandalism resilience. With these benefits, stationary WPT systems have already been implemented at private residences, bus stops, docks, and warehouses with power levels from 3kW to 300kW. However, fast-charging levels up to 400kW are needed to make the charging times of EVs comparable to conventional refueling times [1]. The systems must also meet applicable regulatory requirements, such as stray field safety limits and radiated EMI, and fit within the applicable ground clearances and track of vehicles as in Fig. 1. The public exposure magnetic field limit set by the International Commission of Non-Ionizing Radiation Protection (ICNIRP) is 27μTrms in the frequency range of 3kHz – 10MHz [2]. In the SAE's J2954 recommended practice for wireless power transfer, this equates to a 27μT$_{\text{RMS}}$ field limits outside the vehicle extents and within the vehicle in the frequency range of 79kHz-90kHz [3].

The design of WPT systems to meet specifications such as power level, coupling, airgap, misalignment tolerance, stray field, and efficiency requires the computation of the fields and inductances of various coil geometries. This is often accomplished with finite element analysis (FEA) approaches [4] or analytical methods [5]. In either case, a candidate, parameterized coil geometry must be defined before the design process begins, limiting the scope of coil geometries considered in the design. Complex coil geometries such as bipolar coils [6], [7], and coils with shielding turns [5] have been shown to enable higher power levels under stray field limits. However, attempting to consider all possible coil geometries, as well as other design parameters such as operating frequency, number of turns, and conductor types, results in a near-intractable design space. With rising numbers of iterations needed, optimization with FEA-based methods that rely on brute-force iterations with full or partial 3D-modeling becomes increasingly computationally expensive. Likewise, many analytical methods are pertinent only to circular or rectangular coils and are not general enough to model a large

range of possible geometries. This work seeks to develop a coil design methodology which is not constrained by pre-defined geometric templates, broadening the scope of design optimization in WPT systems.

The Fourier Analysis Method (FAM) is a promising candidate to meet this challenge. In the Fourier Analysis Method (FAM), the coil fields are first designed to optimize performance through variation of Fourier basis function coefficients. The computed fields are then discretized into winding geometries, without constraint on winding shape. This allows for the rapid computation of the coil conductor geometry, coil inductances, currents, and fields. The FAM is used to develop a convenient, fast method to optimize coil geometry for given stray field and power level specifications.

Magnetic component design using Fourier basis functions is well-known in the design of MRI gradient coils [8], [9], and electric machines [10]. The coil design problem is ill-poised because there is an infinite number of possible current distributions on a plane that can create a given field at a distance. However, the problem can be regularized to have one unique solution when objectives such as minimum power dissipation or stored energy are considered. In general, several basis functions types are possible such as triangular basis functions and Fourier basis functions [8]. However, most coil designs exhibit symmetry such that the number of sinusoidal or Fourier basis functions needed will be lower, reducing the

matrix sizes, number of iterations, and overall computational time.

II. THE FOURIER ANALYSIS METHOD

The FAM works by modeling the scalar magnetic potential of the coil as a function of the coefficients of Fourier basis functions. These functions are two-dimensional sinusoidal functions of different spatial wavelengths in the Cartesian x-y plane. As illustrated in Fig. 1, each basis function is defined by spatial wavenumbers k_x and k_y in the x and y-directions, in units of radians per meter. As later shown, the wavenumber in the z-direction, k_z, is a function of k_x and k_y. These wavenumbers are defined by $k = 2\pi/\lambda$ where λ is the wavelength of the sinusoidal function. The four basis function sets considered in the FAM shown in Fig. 2 are combinations of the sine and cosine functions . In the FAM, an $N \times N \times 4$ matrix of coefficients is used as the optimization variable. Each $N \times N \times 1$ matrix represents the first quadrant of a basis function set and can be used with or independently of the others. To compute the full Fourier-domain matrix of the coil shape, each $N \times N \times 1$ matrix is multiplied and reflected according to the symmetry conditions of Fig. 2a to create a $(2N-1) \times (2N-1)$ matrix. The summation of these matrices yield the Fourier-domain coefficients $\psi(k_x, k_y) = \psi(m, n)$ of the coil shape. The scalar magnetic potential in the spatial
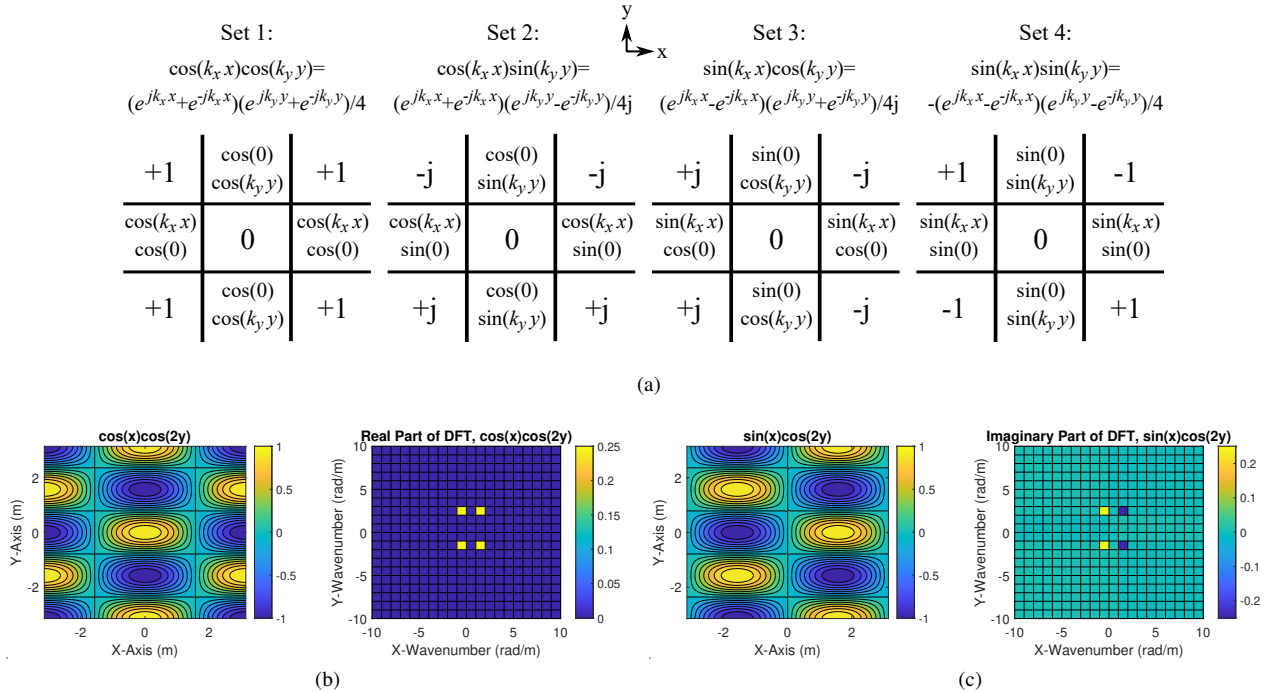

Fig. 2: Diagram of the 4 Basis Functions sets considered in the Fourier Analysis Method. The 4 sets are combinations of sines and cosine functions in two dimensions, each governed by corresponding symmetry conditions. (a) The symmetry conditions for each basis function set comprised of real and complex conjugate relationships. (b) Example plot and coefficients of the $\cos k_x x \cos k_y y$ basis function with $k_x = 1$ rad/m and $k_y = 2$ rad/m. (c) Example plot and coefficients of the $\sin k_x x \cos k_y y$ basis function with $k_x = 1$ rad/m and $k_y = 2$ rad/m.

domain, $\Psi(x, y, z)$, is the Inverse Discrete Fourier Transform (IDFT) of this matrix,

$$\Psi(x, y, z) = \sum_{m=1}^{2N-1}\sum_{n=1}^{2N-1} \psi(m,n)e^{j(k_x x + k_y y + k_z z)})/4. \quad (1)$$

The potentials in the X-Y plane are calculated with a discretization in the x and y dimensions of dx and dy respectively.

A. Field and Current Computation

In the Fourier domain, the basis functions can be directly differentiated or integrated to obtain algebraic relationships between the potential Ψ and the field $\boldsymbol{B}$ by the relationship $\boldsymbol{B} = \mu_0 \boldsymbol{H} = -\mu_0 \nabla \Psi$. Neglecting displacement current in quasi-magnetostatic conditions, the wavenumber k_z is derived by observing that $\nabla \times \boldsymbol{B} = 0$ in the absence of airgap currents. Combined with $\nabla \cdot \boldsymbol{B} = 0$, the fields and potentials satisfy

$$\nabla^2 \Psi = \nabla^2 \boldsymbol{B} = 0. \quad (2)$$

Therefore, when real, non-zero wavenumbers exist in the x and y-directions, k_z is imaginary and is

$$k_z = \pm\sqrt{-k_x^2 - k_y^2} = \pm j\gamma. \quad (3)$$

The magnetic potential in the airgap must satisfy

$$\frac{\partial^2 \Psi}{\partial z^2} - k_x^2 \Psi = 0 \quad (4)$$

which has solution

$$\Psi(z) = c_1 e^{-\gamma z} + c_2 e^{\gamma z}. \quad (5)$$

The constants c_1 and c_2 are found using the boundary conditions at $\Psi(0)$ and $\Psi(z_{gap})$, yielding the relationship derived in [10]

$$\Psi(z) = \frac{\sinh \gamma z}{\sinh \gamma z_{gap}}\Psi(z_{gap}) - \frac{\sinh \gamma (z - z_{gap})}{\sinh \gamma z_{gap}}\Psi(0). \quad (6)$$

By differentiating this with $\boldsymbol{B} = \mu_0 \boldsymbol{H} = -\mu_0 \nabla \Psi$, the B_z field at $z = 0$ and $z = z_{gap}$ are

$$\begin{bmatrix} B_z(z_{gap}) \\ B_z(0) \end{bmatrix} = -\mu_0\gamma \begin{bmatrix} \coth \gamma z_{gap} & -\frac{1}{\sinh \gamma z_{gap}} \\ \frac{1}{\sinh \gamma z_{gap}} & -\coth \gamma z_{gap} \end{bmatrix} \begin{bmatrix} \Psi(z_{gap}) \\ \Psi(0) \end{bmatrix} \quad (7)$$

For a discrete set of spatial frequencies, the fields at the secondary coil, where $z = z_{gap}$, due to the potential of the primary coil varying in the x and y plane at $z = 0$, are a function of z_{gap} and $\gamma = \sqrt{k_x^2 + k_y^2}$ for ferrite backed coils as in (8)-(10). As this calculation determines the fields from the primary coil only, it is assumed that no currents are present in the secondary coil such that $\Psi(z_{gap}) = 0$ in (7).

$$B_x(x, y, z_{gap}) = \sum_{m=1}^{2N-1}\sum_{n=1}^{2N-1} \frac{-\mu_0 j k_x \psi(m,n)e^{j(k_x x + k_y y)}}{4 \sinh \gamma z_{gap}} \quad (8)$$

$$B_y(x, y, z_{gap}) = \sum_{m=1}^{2N-1}\sum_{n=1}^{2N-1} \frac{-\mu_0 j k_y \psi(m,n)e^{j(k_x x + k_y y)}}{4 \sinh \gamma z_{gap}} \quad (9)$$

$$B_z(x, y, z_{gap}) = \sum_{m=1}^{2N-1}\sum_{n=1}^{2N-1} \frac{-\mu_0 j \gamma \psi(m,n)e^{j(k_x x + k_y y)}}{4 \sinh \gamma z_{gap}} \quad (10)$$

For air-core coils, the fields will be half or less as the magnetic path lengths are double or more than in ferrite backed coils. Here, the boundary conditions $\Psi(z) = 0$ occur at infinity.

$$\begin{bmatrix} B_z(z_{gap}) \\ B_z(0) \end{bmatrix} = -\mu_0\gamma \begin{bmatrix} 1/2 & -e^{-\gamma z_{gap}} \\ e^{-\gamma z_{gap}} & -1/2 \end{bmatrix} \begin{bmatrix} \Psi(z_{gap}) \\ \Psi(0) \end{bmatrix} \quad (11)$$

By (6)-(11), fields with higher k_x and k_y, i.e. with shorter wavelengths, will decrease in magnitude faster in the z-direction than those with smaller k_x and k_y. In short, the near-field scattering phenomenon describes how coils with larger diameters have fields that decay more slowly away from the coil surface than those of smaller coils.

The potentials of the coils are determined by currents flowing in the plane of the coil. The continuous surface currents in the x and y-direction are K_x and K_y

$$\boldsymbol{K} = \nabla \times \hat{\boldsymbol{k}}\Psi = \frac{\partial \Psi}{\partial y}\hat{\boldsymbol{i}} - \frac{\partial \Psi}{\partial x}\hat{\boldsymbol{j}} \quad (12)$$

$$K_x(x, y, 0) = \sum_{m=1}^{2N-1}\sum_{n=1}^{2N-1} jk_y \psi(m,n)e^{j(k_x x + k_y y)})/4 \quad (13)$$

$$K_y(x, y, 0) = \sum_{m=1}^{2N-1}\sum_{n=1}^{2N-1} -jk_x \psi(m,n)e^{j(k_x x + k_y y)})/4. \quad (14)$$

B. Computation of Coil Inductance, Current, and Power

The mutual and self magnetic energies, E_m and E_s respectively, are

$$E_m(\psi) = \int_\Omega \Psi(x, y, 0)B_z(x, y, z_{gap})d\Omega \quad (15)$$

$$E_s(\psi) = \frac{1}{2}\int_\Omega \Psi(x, y, 0)B_z(x, y, 0)d\Omega. \quad (16)$$

These energy values are related to the total magnetic energy of the system W

$$W = E_{s1}(\psi) + E_{s2}(\psi) = \frac{1}{2}L_1 I_1^2 + \frac{1}{2}L_2 I_2^2 + MI_1 I_2. \quad (17)$$

Assuming matched coils with $L_1 = L_2$ operating with coil RMS currents of $I_1 = I_2$, the equivalent coupling coefficient k of the system is

$$k = \frac{E_m(\psi)}{2E_s(\psi)} = \frac{\int_\Omega \Psi(x, y, 0)B_z(x, y, z_{gap})d\Omega}{\int_\Omega \Psi(x, y, 0)B_z(x, y, 0)d\Omega}. \quad (18)$$

By choosing the number of turns of the coil, N_T, the conductor paths, currents, and coil shape are determined by the contours C of the continuous magnetic potential

$$I_1 = (\max \Psi(x, y, 0) - \min \Psi(x, y, 0))/N_T \quad (19)$$

$$C = \min \Psi(x, y, 0)) + (0 : (N_T - 1) + \frac{1}{2})I_1. \quad (20)$$

Equation (17) is used to calculate L_1 and L_2 and the mutual inductance of the system, M, once I_1 and I_2 are determined. The coil-to-coil power transfer of the system, P, is then

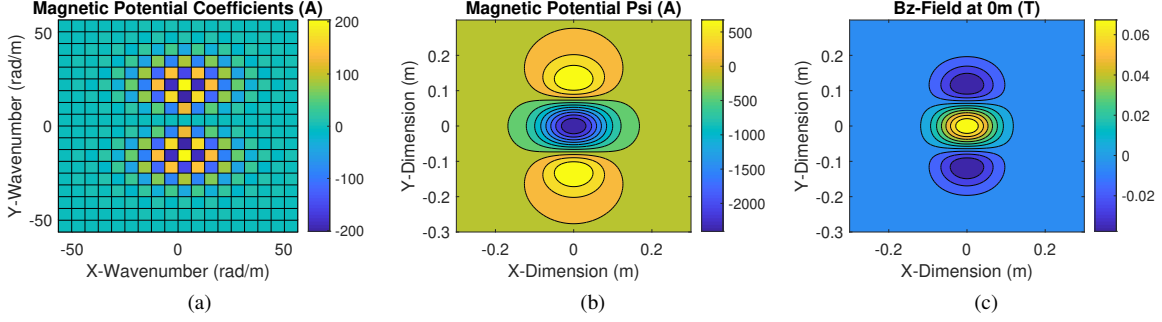$$P = 2\pi f E_m(\psi) = 2\pi f MI_1 I_2. \quad (21)$$

Fig. 3: (a) Basis function coefficients $\psi(m,n)$ (b) magnetic scalar potential and (c) surface B_z field of one ferrite coil from the FAM with an airgap of $z_{gap} = 0.2$m and a coil to coil power transfer of 20kW at 85kHz.

TABLE I: Comparison of FAM, FEA, and Experimental Measurements of Inductance $N_T = 14$

Parameter	Ferrite-Backed Coil		Air-Core Coil		
	FAM (Continuous)	FEA (Windings)	FAM (Continuous)	FEA (Windings)	Experimental Measurements
Self Inductance L_1, L_2	30.64μH	31.01μH	15.32μH	16.15μH	16.56μH, 16.20μH
Mutual Inductance M	1.31μH	1.27μH	0.32μH	0.31μH	0.31μH

C. Load Impedance Sensitivity

The assumption that the primary and secondary currents are equal, $I_1 = I_2$, assumes that the coils are matched and are operating at resonance close to the optimal load. With an equivalent AC load resistance on the secondary side, R_L, and parasitic resistances in primary and secondary coils of R_1 and R_2, respectively, a compensated, series-series WPT system is modeled by

$$\begin{bmatrix} V_1 \\ 0 \end{bmatrix} = \begin{bmatrix} R_1 & -j\omega M \\ -j\omega M & R_2 + R_L \end{bmatrix} \begin{bmatrix} I_1 \\ I_2 \end{bmatrix}. \tag{22}$$

Solving this circuit for the output power $P_{out} = I_2^2 R_L$ and dividing by the input power $P_{in} = V_1 I_1$, the efficiency is

$$\frac{P_{out}}{P_{in}} = \frac{I_2^2 R_L}{V_1 I_1} = \frac{(\omega M)^2 R_L}{(R_L + R_2)[(\omega M)^2 + R_1(R_L + R_2)]} \tag{23}$$

which is maximized by optimal loading resistance [11]

$$R_{L,opt} = R_2\sqrt{1 + (\omega M)^2/R_1 R_2}. \tag{24}$$

For matched coils, $R_1 = R_2$ and the optimal load resistance approximates ωM. When operating with a load close to $R_{L,opt}$, the phase of the input impedance is relatively flat with frequency around resonance, such that current does not become inductive with a small increase in frequency above resonance to ensure the soft-switching of the inverter. This is avoided by setting R_L slightly above $R_{L,opt}$, but I_1 will still approximate I_2 for matched coils.

D. Inductance and Field Model Validation

To validate the modeling of the fields and inductances of coils with FAM, a pair of ferrite coils with extents of $x_{ext} = 0.3$m and $y_{ext} = 0.5$m and airgap of $z_{gap} = 0.2$m were designed as in Fig. 3. The potentials and fields are shown with a coil-coil power transfer of 20kW at 85kHz and
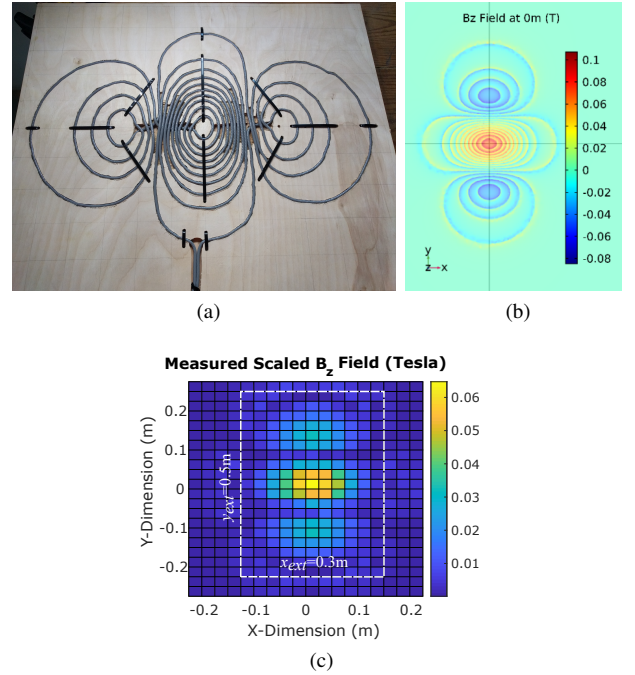

Fig. 4: (a) Constructed air-core coil and (b) FEA simulation of the coil. (c) Scaled measured magnitude of the B_z field.

were determined by a similar optimization methodology as in Section III. The output is a three-pole field shape centered on the origin that consists of only $\cos x \cos y$ basis functions.

The contours of the magnetic potential of Fig. 3b with $N_T = 14$ at values of C are derived and are used to build air-core coils as in Fig. 4a with 10AWG Litz wire. Inductance measurements of the coils were taken on a Keysight E4990A impedance analyzer. The inductance values from the FAM,

FEA simulations, and experimental measurements are given in Table I. As seen, the inductance values derived from the FAM method are within 5% of the FEA results and 7% of the measurements. The FEA simulation result of the fields is shown in Fig. 4b. Field measurements of B_z at the surface of the coil were taken with a sensing coil 31mm in diameter with 45 turns of 24 AWG magnet wire and are plotted in Fig. 4c. The comparison of the model fields and inductance to the measured values demonstrate that the FAM can accurately predict the inductance, coupling, and field distribution for the output.

III. OPTIMIZATION OF STRAY FIELD AND CURRENT

Using the FAM, a multi-objective optimization is formulated and solved to design coil geometries with objectives and constraints based on minimizing the total current in the coil while limiting the stray field maximum outside the coil extent. Each objective and constraint is normalized to scale derivatives to similar values to assist the convergence of gradient-based solvers.

The optimization is formulated as minimization of the surface integral of the total current in the coil structure squared, $\int_\Omega K(x,y,0)^2 d\Omega$. The surface integral

$$\int_\Omega K(x,y,0)^2 d\Omega = (||K_x(\psi)||_2^2 + ||K_y(\psi)||_2^2)/16 \quad (25)$$

is calculated by noting that the Fourier transform is a unitary function. This avoids the computation of $K(x,y,0)$ in each objective function evaluation step. The 1-norm of the magnitude of the basis function coefficient ψ is added to eliminate small values of unused basis function sets such as $\sin 0 \cos y$ as given in Fig. 2 yielding the objective function

$$\frac{||K_x(\psi)||_2^2 + ||K_y(\psi)||_2^2}{16P} + 0.1\frac{||\psi||_1}{P} \quad (26)$$

The first constraint is the coil-coil power transfer computed using (21)

$$(P - 2\pi f E_m(\psi))/P \leq 0. \quad (27)$$

The next constraint is the maximum average stray field magnitude $B_{str,lim}$ in the airgap outside the measurement extents x_{meas} and y_{meas}.

$$(||B_{str,avg}(x,y)||_{50} - B_{str,lim})/B_{str,lim} \leq 0 \quad (28)$$

The inclusion of the stray field as a constraint ensures the compliance of the system with safety standards on public magnetic field exposure. This is computed as the 50-norm of the spatial stray-field matrix which approximates the infinity norm or maximum magnitude of the matrix. $B_{str,avg}$ is the average field magnitude outside the measurement extents x_{meas} and y_{meas} and is computed similar to B_{avg} in (32). The average of the fields in the airgap is derived by integrating the contribution from each basis function from $z=0$ to $z=z_{gap}$ and dividing by z_{gap} to obtain the average field in the airgap,

$$B_{x,avg}(x,y) = \sum_{m=1}^{2N-1}\sum_{n=1}^{2N-1} \frac{-\mu_0 jk_x\psi(m,n)e^{j(k_x x + k_y y)}}{\gamma z_{gap}} \quad (29)$$

$$B_{y,avg}(x,y) = \sum_{m=1}^{2N-1}\sum_{n=1}^{2N-1} \frac{-\mu_0 jk_y\psi(m,n)e^{j(k_x x + k_y y)}}{\gamma z_{gap}} \quad (30)$$

$$B_{z,avg}(x,y) = \sum_{m=1}^{2N-1}\sum_{n=1}^{2N-1} \frac{-\mu_0 \gamma\psi(m,n)e^{j(k_x x + k_y y)}}{\gamma z_{gap}}. \quad (31)$$

The average field magnitude $B_{avg}(x,y)$, is then

$$B_{avg}(x,y) = \sqrt{B_{x,avg}(x,y)^2 + B_{y,avg}(x,y)^2 + B_{z,avg}(x,y)^2}. \quad (32)$$

The third constraint limits the continuous current density to the desired coil extents x_{ext} and y_{ext} such that the surface integral of the stray current squared, $\int_\Omega K_{str}(x,y,0)^2 d\Omega$, is a small percentage, $\alpha = $ 1e-4, of the surface integral of the total current $\int_\Omega K(x,y,0)^2 d\Omega$.

$$\frac{\int_\Omega K_{str}(x,y,0)^2 d\Omega - \alpha \int_\Omega K(x,y,0)^2 d\Omega}{\int_\Omega K(x,y,0)^2 d\Omega} \leq 0 \quad (33)$$

In summary, the objective function and constraints form the optimization

$$\min \left(\frac{||K_x(\psi)||_2^2 + ||K_y(\psi)||_2^2}{16P} + 0.1\frac{||\psi||_1}{P} \right)$$

$$\text{s.t.}$$

$$(P - 2\pi f E_m(\psi))/P \leq 0, \quad (34)$$

$$(||B_{str,avg}(x,y)||_{50} - B_{str,lim})/B_{str,lim} \leq 0,$$

$$\frac{\int_\Omega K_{str}(x,y,0)^2 d\Omega - \alpha \int_\Omega K(x,y,0)^2 d\Omega}{\int_\Omega K(x,y,0)^2 d\Omega} \leq 0.$$

A. Optimization Outputs, Tradeoff of Current and Stray Field

For $B_{str,lim}$ of 5μT to 1mT the optimization of (34) was solved using $x_{ext} = 0.7$m and $y_{ext} = 0.5$m with an airgap of $z_{gap} = 0.2$m, coil-coil power of $P = 6.6$kW, and frequency of $f = 85$kHz. The measurement extents were $x_{meas} = 0.8$m and $y_{meas} = 0.6$m such that the stray fields are measured at a distance of 5cm from the coil extent. The design space dimensions are $D_x = D_y = 1.4$m with discretization
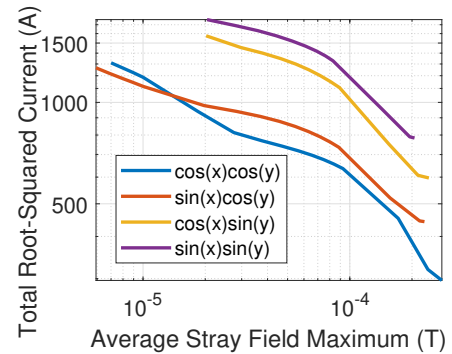

Fig. 5: The maximum average stray field magnitude for the optimized coils vs. the square root of the integral of the current magnitude squared over a range of $B_{str,lim}$ of 5μT to 1mT.

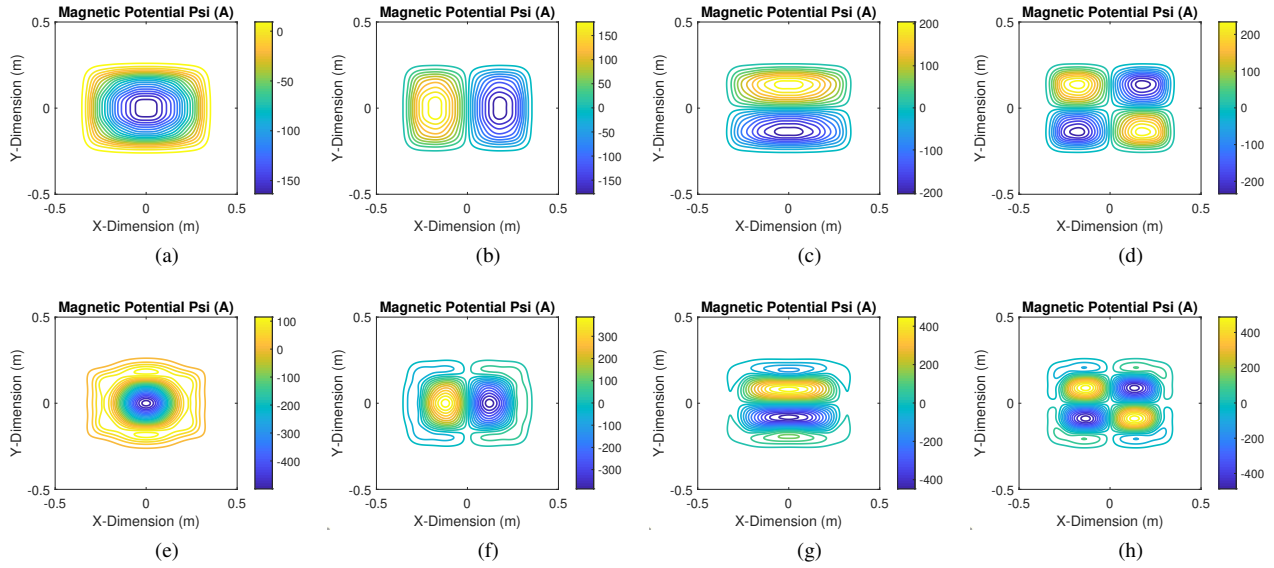Fig. 6: Plots of coil contours from each basis function for $x_{ext} = 0.7$m and $y_{ext} = 0.5$m when constrained by $B_{str,max} = 1$mT with a number of turns $N_T = 20$. (a) A rectangular coil from the $\cos x \cos y$ set. (b) A bipolar coil in the x-direction from the $\sin x \cos y$ set. (c) A bipolar coil in the y-direction from the $\cos x \sin y$ set. (d) A 4-pole coil from the $\sin x \sin y$ set. Plots when constrained by $B_{str,max} = 20$μT with a number of turns $N_T = 24$. (e) A shielded rectangular coil from the $\cos x \cos y$ set. (f) A shielded bipolar coil in the x-direction from the $\sin x \cos y$ set. (g) A shielded bipolar coil in the y-direction from the $\cos x \sin y$ set. (h) A shielded 4-pole coil from the $\sin x \sin y$ set.
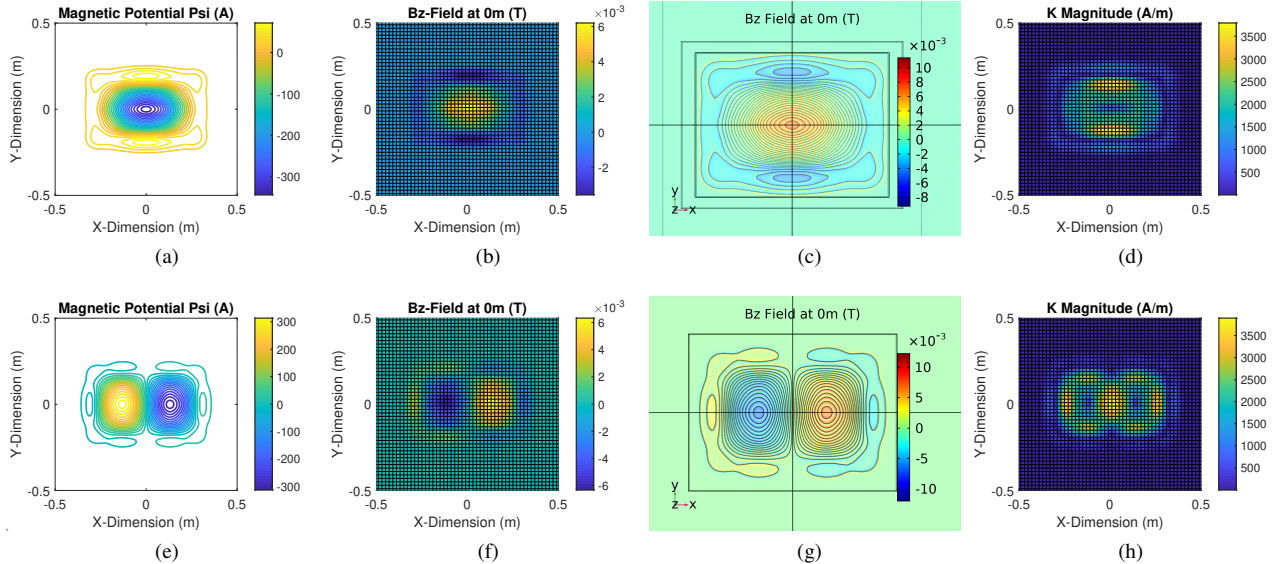

Fig. 7: Points from the optimization where $B_{str,max} = 100$μT shown when $f = 85$kHz and $P = 6.6$kW. (a) Coil structure from the $\cos x \cos y$ set with $N_T = 25$. (b) Discretized surface field of the $\cos x \cos y$ coil shape. (c) FEA output of the $\cos x \cos y$ coil. (d) Surface current magnitude of the $\cos x \cos y$ coil. (e) Coil structure from the $\sin x \cos y$ set with $N_T = 30$. (f) Discretized surface field from the $\sin x \cos y$ coil. (g) FEA output of the $\sin x \cos y$ coil. (h) Surface current magnitude of the $\sin x \cos y$ coil.

$dx = dy = 0.02$m. The spatial wavenumbers k_x and k_y of the basis functions are chosen so that $k_x = m(2\pi/D_x)$ and $k_y = n(2\pi/D_y)$. $N = 15$ so that the optimization variable is a $15 \times 15 \times 4$ matrix of weights when all basis functions are used. With these parameters, each evaluation of (34) took 18.1ms when using all basis functions. The processor is an

Intel Xeon C5-1620 with 80GB of RAM.

The solutions for $B_{str,max}$ of 5µT to 1mT are plotted in Fig. 5. The current magnitude integral is computed as the square root of (25). As seen in Fig. 5, some basis functions did not converge when constrained by field $B_{str,lim}$ values: below $B_{str,lim} = 7$µT for the $\cos x \cos y$ basis function, below $B_{str,lim} = 6$µT for $\sin x \cos y$, and below $B_{str,lim} = 20$µT for $\cos x \sin y$ and $\sin x \sin y$. In these cases, convergence requires basis functions with higher frequencies. With higher numbers of basis functions N, and more iterations, solutions for these points could likely be found. However, these outputs require a relatively high current magnitude and may not be needed to meet stray field specifications. Likewise, with higher stray field limits than 200µT, the stray field limit did not constrain the output compared to the stray current constraint.

As $B_{str,lim}$ is reduced, there is an improvement in the outputs of the $\sin x \cos y$ set over the $\cos x \cos y$ set. Outputs representing combinations of the $\cos x \cos y$ and $\sin x \cos y$ basis functions were possible at this crossover point. It is expected that additional crossover points with other basis function sets will occur as $B_{str,lim}$ is further reduced. It was observed that the optimality of the basis function sets is sensitive to the aspect ratio of the coil used. For example, if x_{ext} is chosen to be smaller than y_{ext}, the $\cos x \sin y$ basis function set required less current overall than the $\sin x \cos y$ basis function set.

The $\cos x \cos y$ basis functions result in rectangular, circular, or other unipolar coil shapes or shapes with odd numbers of poles. The $\sin x \cos y$ and $\cos x \sin y$ basis functions result in bipolar shapes or shapes with even numbers of poles oriented in the x-direction or y-direction respectively. The $\sin x \sin y$ basis function results in coils structures with multiples of four

poles. Examples of each of these for the highest stray field bound for $B_{str,max} = 1$mT are shown in Fig. 6 for a number of turns of $N_T = 20$.

The solutions for $B_{str,lim} = 1$mT in Fig. 6a-6d are dominated by lower frequency wavenumbers with longer spatial wavelengths that have smaller decay in the z-direction. The solutions for $B_{str,lim} = 20$µT shown in Fig. 6e-6h have higher frequency wavenumbers with smaller main poles and have small side-pole structures similar to shielding turns. All solutions in Fig. 6e-6h have total amp-turn values greater than their respective counterparts in Fig. 6a-6d which result in larger total current magnitudes in the coil for the same power transfer level.

B. Analysis of Coil Geometries

Based on the optimization results, the two coil geometries in Fig. 7 were selected for further analysis. These points are from the optimization where $B_{str,max} = 100$µT for the $\cos x \cos y$ basis function and the $\sin x \cos y$ basis function. For a coil-coil power transfer of 6.6kW, the $\cos x \cos y$ coil has $V_1 = 382.3$V and $I_1 = 17.3$A and the $\sin x \cos y$ coil has $V_1 = 305.4$V and $I_1 = 21.6$A. An FEA solver was used to derive the inductance and fields for the 85kHz operating frequency for comparison to the values derived in FAM. The fields at mid-airgap from the two coils geometries from FAM and FEA simulation are shown in Fig. 8. The inductance values derived in FAM versus FEA simulations are given in Table II.

C. Impact of Coil Discretization

When limited to a single-layer coil, the number of turns must be chosen so that the conductors can physically be placed on the surface of the coil in a single layer with wire
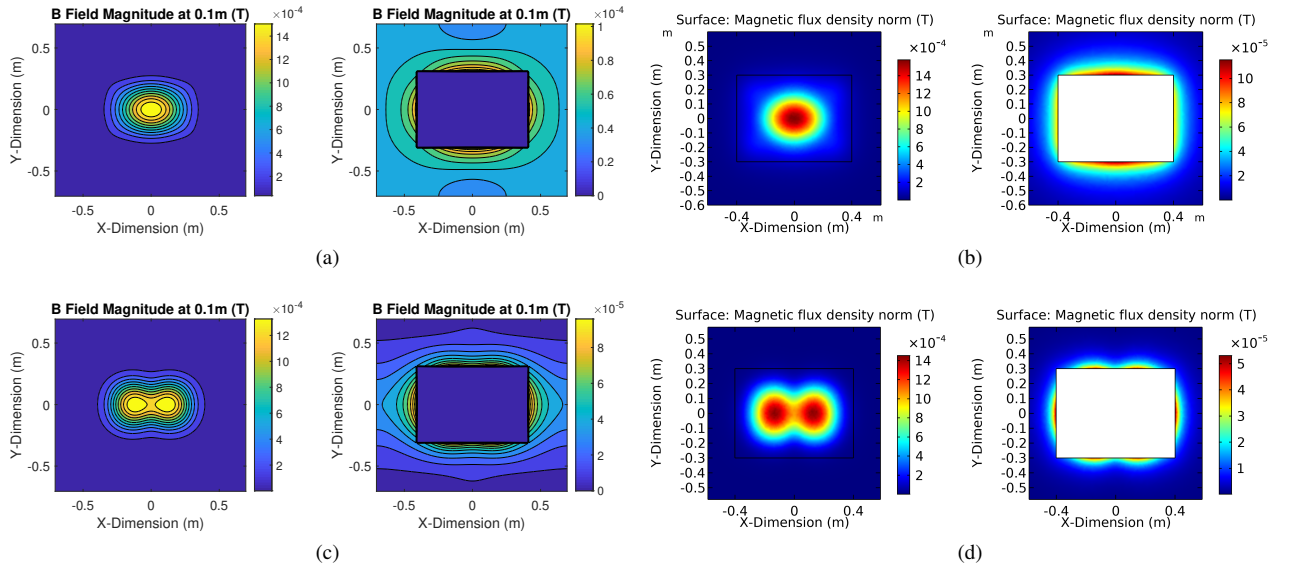

Fig. 8: Fields calculated in FAM and simulated in FEA for the $\cos x \cos y$ coil (a) Calculated field magnitude at $z = 0.1$m for the $\cos x \cos y$ coil. (b) Fields from FEA simulation with one coil energized for the $\cos x \cos y$ coil. (c) Calculated stray field at $z = 0.1$m for the $\sin x \cos y$ coil. (d) Fields from FEA simulation with one coil energized for the $\sin x \cos y$ coil.

TABLE II: Calculated Inductance Values in FAM and FEA

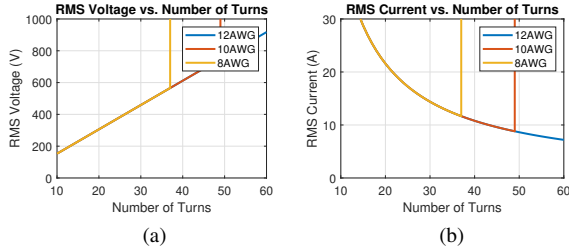| Parameter	FAM	FEA (Windings)	Error (%)
$\cos x \cos y$ Coil			
Self Inductance L_1, L_2	229.6μH	236.8μH	-3.0%
Mutual Inductance M	40.9μH	37.7μH	8.5%
$\sin x \cos y$ Coil			
Self Inductance L_1, L_2	185.5μH	199.2μH	-6.9%
Mutual Inductance M	25.8μH	26.6μH	-3.0%

Fig. 9: Ideal RMS (a) voltage and (b) current for the coil geometry of Fig. 7a at a power level of 6.6kW. In these plots, the voltage or current is set as a large number when condition (35) is violated.

diameters d_{out}. This value is given in datasheets by the wire manufacturer and includes the outer insulation, coating, and conductors. This can be assured by relating the wire diameter and current to the maximum value of $K_{mag}(x, y, 0)$, K_{max}

$$\frac{\max \Psi(x, y, 0) - \min \Psi(x, y, 0))}{N_T d_{out}} = \frac{I_1}{d_{out}} < K_{max}. \quad (35)$$

Since this is dependent on d_{out}, the number of turns that violate this condition varies per gauge of wire. For a given power level, the product of voltage and current remain approximately the same, but the impedance ratio varies based on the selection of N_T. As an example, the coil current and voltage for the coil of Fig. 7a are plotted in Fig. 9. In these plots, multiple Litz wire diameters are considered to illustrate the limitation of (35). Here, larger gauges of wire will be limited to higher I_1 and I_2 than smaller gauges. For example, the selection of smaller gauges of wire and more turns may be favorable to reduce inverter currents when considering the inverter device R_{DS} loss.

CONCLUSION

In this work, the Fourier Analysis Method (FAM) was detailed. The FAM was shown to rapidly and accurately calculate the current, field, power transfer, and inductances and was used to optimize wireless power transfer coil geometries to limit stray field while minimizing the total current norm of the coils at a given power level. The optimization outputs included several coil geometries similar to those in the literature like rectangular or bipolar coils, but also more complex coils with shielding turns that reduce the stray field of the system at the cost of increased current.

As the power levels of systems rise, system optimizations including coil geometries and losses are needed to meet the stray field and efficiency specifications of WPT in electric vehicles. In future work, the FAM could be used to model the efficiency of WPT systems. Many loss mechanisms, such as skin effect and proximity effect conduction losses and ferrite hysteresis losses are dependent on the fields present in the coils and the overall conductor path. Operations such as translation in the Fourier domain are likewise feasible such that the inclusion of misalignment can be included.

REFERENCES

[1] C. J. Michelbacher et al., "Enabling Fast Charging: A Technology Gap Assessment," Idaho National Lab, US Department of Energy, 2017.
[2] ICNIRP, "Guidelines for limiting exposure to time-varying electric and magnetic fields (1 Hz to 100 kHz)," *Health physics*, vol. 99, no. 6, pp. 818-836, 2010.
[3] *Wireless Power Transfer for Light-Duty Plug-In/ Electric Vehicles and Alignment Methodology*, SAE International TIR J2954, 2016.
[4] R. Bosshard, U. Iruretagoyena, and J. W. Kolar, "Comprehensive Evaluation of Rectangular and Double-D Coil Geometry for 50 kW/85 kHz IPT System," *Journal of Emerging and Selected Topics in Power Electronics*, vol. 4, no. 4, pp. 1406-1415, 2016.
[5] T. Campi, S. Cruciani, F. Maradei, and M. Feliziani, "Active Coil System for Magnetic Field Reduction in an Automotive Wireless Power Transfer System," in *2019 IEEE International Symposium on Electromagnetic Compatibility, Signal & Power Integrity*, 2019, pp. 189-192.
[6] J. Pries, V. P. N. Galigekere, O. C. Onar, and G.-J. Su, "A 50-kW Three-Phase Wireless Power Transfer System Using Bipolar Windings and Series Resonant Networks for Rotating Magnetic Fields," *IEEE Transactions on Power Electronics*, vol. 35, no. 5, pp. 4500-4517, 2020.
[7] M. Mohammad, J. L. Pries, O. C. Onar, V. P. Galigekere, G. J. Su, and J. Wilkins, "Comparison of Magnetic Field Emission from Unipolar and Bipolar Coil-Based Wireless Charging Systems," in *2020 IEEE Transportation Electrification Conference & Expo (ITEC)*, 2020, pp. 1201-1207.
[8] M. Poole, P. Weiss, H. S. Lopez, M. Ng, and S. Crozier, "Minimax current density coil design," *Journal of Physics D: Applied Physics*, vol. 43, no. 9, 2010.
[9] G. N. Peeren, "Stream function approach for determining optimal surface currents," PhD Thesis, Technische Universiteit Eindhoven, 2003.
[10] J. R. Melcher, *Continuum electromechanics*. MIT Press. Cambridge, MA, USA. 1981.
[11] Q. Duong and M. Okada, "Maximum Efficiency Formulation for Multiple-Input Multiple-Output Inductive Power Transfer Systems," in *IEEE Transactions on Microwave Theory and Techniques*, vol. 66, no. 7, pp. 3463-3477, July 2018.